In situ bone regeneration of large cranial defects using synthetic ceramic implants with a tailored composition and design

Omar Omar[a,1], Thomas Engstrand[b,c,1], Lars Kihlström Burenstam Linder[d], Jonas Åberg[e], Furqan A. Shah[a], Anders Palmquist[a], Ulrik Birgersson[f], Ibrahim Elgali[a], Michael Pujari-Palmer[e], Håkan Engqvist[e], and Peter Thomsen[a,2]

[a]Department of Biomaterials, Institute of Clinical Sciences, Sahlgrenska Academy, University of Gothenburg, 40530 Gothenburg, Sweden; [b]Stockholm Craniofacial Centre, Department of Molecular Medicine and Surgery, Plastic Surgery Section, Karolinska University Hospital and Karolinska Institutet, 17176 Stockholm, Sweden; [c]Department of Surgical Sciences, Uppsala University, 75185 Uppsala, Sweden; [d]Department of Clinical Neuroscience, Neurosurgical Section, Karolinska University Hospital and Karolinska Institutet, 17176 Stockholm, Sweden; [e]Department of Engineering Sciences, Applied Materials Science Section, Uppsala University, 75121 Uppsala, Sweden; and [f]Division of Imaging and Technology, Department of Clinical Science, Intervention and Technology, Karolinska Institutet, 14152 Huddinge, Sweden

Edited by Robert Langer, Massachusetts Institute of Technology, Cambridge, MA, and approved August 28, 2020 (received for review May 16, 2020)

The repair of large cranial defects with bone is a major clinical challenge that necessitates novel materials and engineering solutions. Three-dimensionally (3D) printed bioceramic (BioCer) implants consisting of additively manufactured titanium frames enveloped with CaP BioCer or titanium control implants with similar designs were implanted in the ovine skull and at s.c. sites and retrieved after 12 and 3 mo, respectively. Samples were collected for morphological, ultrastructural, and compositional analyses using histology, electron microscopy, and Raman spectroscopy. Here, we show that BioCer implants provide osteoinductive and microarchitectural cues that promote in situ bone regeneration at locations distant from existing host bone, whereas bone regeneration with inert titanium implants was confined to ingrowth from the defect boundaries. The BioCer implant promoted bone regeneration at nonosseous sites, and bone bonding to the implant was demonstrated at the ultrastructural level. BioCer transformed to carbonated apatite in vivo, and the regenerated bone displayed a molecular composition indistinguishable from that of native bone. Proof-of-principle that this approach may represent a shift from mere reconstruction to in situ regeneration was provided by a retrieved human specimen, showing that the BioCer was transformed into well-vascularized osteonal bone, with a morphology, ultrastructure, and composition similar to those of native human skull bone.

bioceramic | titanium | 3D printing | cranial reconstruction | osteoinduction

The reconstruction of cranial defects represents a major challenge for the patient, the health care system, and society. Ideally, material introduced into a defect should promote a biological response that results in structural and functional restoration of the defect.

Autologous bone grafts have been the standard for reconstructive treatment. However, the relatively high resorption, protrusion, and infection rates and the high rate of donor-site morbidities still represent major obstacles (1–3). Several alloplastic materials have been introduced as alternatives, including polymethyl methacrylate, polyether ether ketone (PEEK), polyethylene, titanium, and injectable/moldable calcium phosphate-based bone cement. The main drawback of these materials is poor bone and soft tissue integration, which may cause implant exposure, infection, and ultimately, implant removal (4, 5). Although common, cranioplasty results in high complication rates and costs (3, 6), necessitating new biomaterial-based innovative solutions.

A scaffold, cells, and biochemical signals are considered the triad necessary for tissue regeneration (7). Efforts are being made to determine the regenerative potential of these factors alone or in combination. Cell therapy contributes to intramembranous bone formation and significantly increases calvarial defect repair in experimental studies (8, 9). Growth factors have resulted in improved bone regeneration in experimental studies (10, 11). Although

Significance

Large cranial reconstructions are increasingly performed worldwide and still represent a substantial clinical challenge. The gold standard, autologous bone, has limited availability and high donor-site morbidity. Current alloplastic materials are associated with high complication and failure rates. This study shows the capacity of a customized, purely synthetic, 3D-manufactured bioceramic implant to regenerate and restore large cranial defects with mature, well-vascularized bone, with a morphology, ultrastructure, and composition similar to those of native skull bone. This approach triggers the regenerative potential of host tissue by tailoring the implant composition and design. The regeneration of large defects using purely synthetic material without adjunct cell therapy or growth factors represents a major advancement for rehabilitating patients in need of large cranial reconstructions.

Author contributions: O.O., T.E., L.K.B.L., J.Å., U.B., H.E., and P.T. designed research; O.O., T.E., L.K.B.L., J.Å., F.A.S., A.P., U.B., I.E., M.P.-P., H.E., and P.T. performed research; M.P.-P. contributed new reagents/analytic tools; O.O., J.Å., F.A.S., A.P., I.E., M.P.-P., and P.T. analyzed data; O.O., T.E., L.K.B.L., J.Å., F.A.S., A.P., H.E., and P.T. interpreted data; and O.O., T.E., F.A.S., U.B., and P.T. wrote the paper.

Competing interest statement: The study was supported by the BIOMATCELL VINN Excellence Center of Biomaterials and Cell Therapy, the Västra Götaland Region, the Swedish Research Council (2018-02891 and 2017-04728), the Swedish Foundation for Strategic Research (RMA15-0110), the Swedish state under the agreement between the Swedish government and the county councils, the ALF agreement (ALFGBG-725641), the IngaBritt and Arne Lundberg Foundation, the Hjalmar Svensson Foundation, the Adlerbertska Foundation, the Sylvan Foundation, and the Area of Advance Materials of Chalmers and GU Biomaterials within the Strategic Research Area initiative launched by the Swedish government. The funding sources had no role in the conceptualization, design, data collection, analysis, decision to publish, or preparation of the manuscript. All listed funding sources provided research grants that covered materials, consumables, equipment, and the salaries of the University of Gothenburg (O.O., F.A.S., A.P., I.E., and P.T.) and University of Uppsala (M.P.-P. and H.E.) employees. P.T. is a shareholder of OssDsign AB. T.E., J.Å., and H.E. serve as consultants with OssDsign AB, are shareholders of OssDsign AB, and have two patents (US20130066324A130 and US9220597B232) relevant to this work. L.K.B.L. serves as a study executor and educational consultant at OssDsign AB and has a stock option with OssDsign AB. U.B. is employed by OssDsign AB and has employee stock options.

This article is a PNAS Direct Submission.

[1]O.O. and T.E. contributed equally to this work.

[2]To whom correspondence may be addressed. Email: peter.thomsen@biomaterials.gu.se.

This article contains supporting information online at https://www.pnas.org/lookup/suppl/doi:10.1073/pnas.2007635117/-/DCSupplemental.

First published October 12, 2020.

promising, these strategies are still in the developmental stage, and the regeneration of large, cranial defects in humans has thus far attracted limited attention. Unsatisfactory clinical results have been achieved with autologous adipose-derived stem cells in combination with β-tricalcium phosphate (β-TCP) granules and titanium or polymer mesh (12). Encouraging results have been obtained with the combination of bone morphogenetic protein-2 (BMP-2), collagen sponges, and polylactide plates in a small group of patients (13). Nevertheless, the latter strategy is largely hampered by potential long-term adverse events and by regulatory and financial constraints (14–16).

The process of bone regeneration in conjunction with biomaterials has been extensively documented, and several terms have been coined, including osseointegration, osteoconduction, and osteoinduction. Osseointegration has been defined as the integration of a screw-shaped titanium implant with direct bone contact (17), withstanding the functional load (18) without loosening (19). Osteoconduction refers to bone growth on a surface; hence, an osteoconductive material allows bone growth on its surface or into pores, channels, or irregularities (20). The term osteoinduction generally refers to the induction of undifferentiated osteoprogenitor cells to commit to the osteogenic lineage (21). In the context of biomaterials, Miron and Zhang (22) listed mesenchymal stem cell (MSC) recruitment, MSC differentiation to osteoblasts, and ectopic bone formation as crucial principles for osteoinduction. Daculsi et al. (20) defined osteoinduction as active osteoinduction (as with BMP) or passive osteoinduction (if a material/scaffold is able to induce osteogenic differentiation). More recently, Bohner and Miron (23) used the term intrinsic osteoinduction to describe material-induced heterotopic ossification. Although the definitions and mechanisms of these processes are incompletely understood, it could be hypothesized that an ideal implant for large defects should allow for osteoconduction and have osteoinductive capacity while being able to establish long-term osseointegration in the recipient bone defect.

For large bone defects, a composite implant comprising mechanically robust and bioactive components provides an appropriate alternative. In this case, titanium would be an excellent reinforcing material that is well documented for osseointegration and osteoconduction (24, 25). Several CaP-based ceramics are known to promote bone regeneration. Monetite is the anhydrous form of dicalcium phosphate, with a relatively high rate of bioresorbability, and in vivo studies have revealed its bone-promoting effect (26–28). Moreover, monetite, with controlled open and closed channel geometries, demonstrated osteoconduction and osteoinduction when implanted in skeletal and nonskeletal sites in a goat model (29). Additionally, intentional inclusion of other CaP phases may not only modify mechanical and handling properties but may also modify osteoinductive effects. For example, it has been shown that the addition of small amounts of β-TCP and pyrophosphate improves the mechanical properties (30) and setting time (31), respectively, of calcium phosphate cements. Moreover, the presence of the β-TCP phase together with hydroxyapatite (HA) in biphasic ceramic provided osteoinductive and bone-promoting effects in vivo, which were not evident with either phase implanted alone (32, 33). The advent of three-dimensional (3D) imaging, computer-assisted design, and additive manufacturing technologies has provided new opportunities, enabling the manufacture of customized composite implants (34, 35).

This study focuses on the hypothesis that cranial defects in humans can be repaired by an implant tailored to promote bone regeneration and osseointegration in the entire defect. Such an implant should recapitulate the shape of the cranial vault, exhibit sufficient mechanical properties, promote vascularization and tissue ingrowth via multiple interconnected spaces, facilitate host cell recruitment via osteoconductive and osteoinductive material properties, and be replaced by bone. The approach reported here does not employ the systemic or local application of cells or growth factors. Using 3D-printed cranial implants consisting of a titanium-reinforced bioceramic (BioCer), we report the long-term (12 mo) repair of surgically created cranial defects with mature, well-vascularized bone and associated periosteum and endosteum in sheep. Proof-of-principle that large, hemicraniectomies in humans can be restored by new bone, with a structure and composition similar to that of normal bone, was provided after the detailed investigation of a retrieved, customized BioCer implant 21 mo postsurgery.

Results

Implant Design and Characterization. The experimental BioCer implant (test) used in the sheep skull was composed of calcium phosphate tiles reinforced and interconnected by an additively manufactured titanium frame with built-in, low-profile fixation arms (Fig. 1*A*). The titanium (Ti) implant (control) used in the sheep skull had a design and dimensions similar to those of the BioCer implant, but it was made entirely of additively manufactured Ti (grade 23) (Fig. 1*B*). The BioCer cranial implant used in the human skull was composed of calcium phosphate tiles interconnected by a Ti frame, with built-in fixation arms for anchorage of the implant to the recipient, native skull bone (Fig. 1*C*). The top and bottom faces of the Ti control were solid, whereas the bulk of the tile was porous (porosity, ∼75%; pore size, ∼0.6 mm).

The amount of glycerol released from the ceramic was 0.25% of the weight of the ceramic in the first extraction, and 0.01% in the second one. In the third consecutive extraction, the amount released, if any, was below the detection limit.

For both the experimental and clinical BioCer implants, X-ray diffraction (XRD) analysis after autoclaving demonstrated that the composition was dicalcium phosphate anhydrous (monetite, 84.74%), β-TCP (8.34%), and dicalcium pyrophosphate (β-CPP, 6.77%) (Fig. 1*D* and *SI Appendix*, Table S1). The XRD analysis also demonstrated that only extremely limited fractions of the material were converted to HA (0.11%) and brushite (0.04%) after autoclaving (Fig. 1*D* and *SI Appendix*, Table S1).

The BioCer implant exhibited a porosity of ∼43%, density of ∼2.6 g/cm^3, and surface area of ∼4 m^2/g. Scanning electron microscopy (SEM) showed that the BioCer tiles consisted of micrometer-sized crystals. The crystals were arranged in a stochastic manner (Fig. 1*E*), giving rise to microporosities within the tile (<1 μm) (Fig. 1 *E* and *F*). The tiles were arranged with grooves/channels of up to 800 μm between adjacent tiles.

Promotion of Bone Regeneration in Sheep Cranial Defects. After 12 mo, BioCer implants revealed defect restoration and soft tissue adaptation in sheep cranial defects. In contrast, soft tissue contraction was apparent around Ti implants, with visible metal on the skin and dura sides (Fig. 2 *A*–*C*).

Histologically, the Ti implants showed less bone than the BioCer implants. Osteonal bone extended from the original recipient bone toward the peripheral interconnected pores (Fig. 2 *D*, *F*, and *H*). The BioCer implants revealed a considerable amount of osteonal bone filling the defects and enveloping and in direct contact with the BioCer tiles (Fig. 2 *E*, *G*, *I*, and *K*). More bone had formed toward the dura side than the skin side (Fig. 2*G*). Within multiple concavities of the partially degraded ceramic, coupling of bone formation and resorption was observed. At these remodeling sites, blood vessels were commonly detected. One conspicuous feature was the regeneration of periosteal and endosteal tissues in the BioCer-treated defects. The corresponding regions of the Ti implants, however, exhibited a thick fibrous encapsulation.

Significantly higher percentages of bone area (BA%) and bone–implant contact (BIC%) were demonstrated for BioCer vs. Ti, both in the total defect area (Fig. 2 *M* and *N*) and in the peripheral and central regions of interest (ROIs) (Fig. 2 *O* and *P*). Very low BIC% values were found for Ti (center, 3%; periphery,

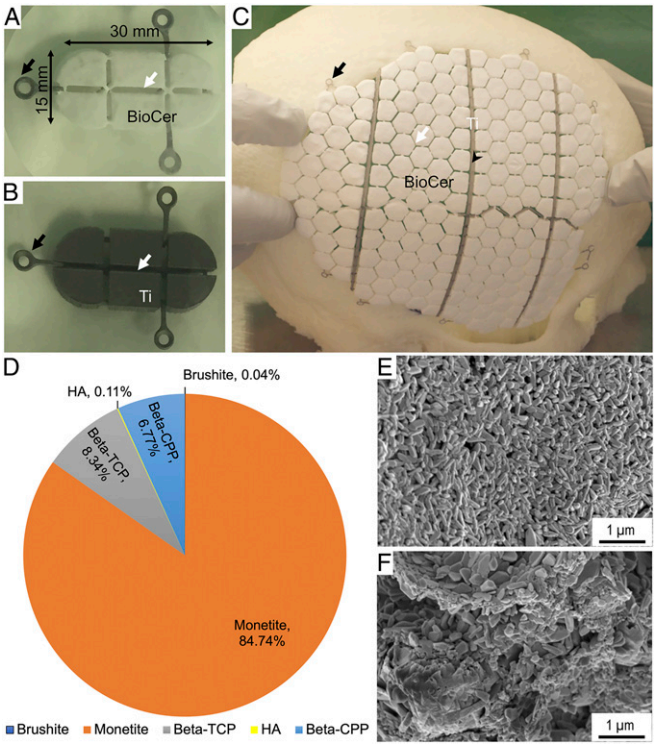

Fig. 1. Design and characterization of the implants. (*A*) The experimental bioceramic (BioCer) implant used in the sheep skull was composed of calcium phosphate tiles reinforced and interconnected by an additively manufactured titanium frame with built-in, low-profile fixation arms (black arrows). The intertile space is indicated (white arrow). (*B*) The titanium (Ti) implant (control) used in the sheep skull had a design and dimensions similar to those of the BioCer but was made entirely of additively manufactured Ti (grade 23). (*C*) The BioCer cranial implant used in the human skull was composed of calcium phosphate tiles interconnected by a Ti frame, with built-in fixation arms (black arrows) for anchorage to the recipient, native skull bone. The clinical implant had the following characteristics. (*i*) Laser-cut, medical grade 2 Ti rectangular frames were welded together and then molded with BioCer tiles. The spacing (white arrow) was 0.5 to 1 mm between two adjacent BioCer tiles. (*ii*) The joints (transitional zone) between two adjacent frames were not covered by the BioCer material and were spaced at 1.5 to 2 mm (black arrowhead), with exposed Ti between two adjacent tiles. (*D*) For both the experimental and clinical BioCer implants after autoclaving, the composition was anhydrous dicalcium phosphate (84.74%), β-TCP (8.34%), and dicalcium pyrophosphate (6.77%), whereas extremely limited fractions of the material were HA (0.11%) and brushite (0.04%) phases. (*E* and *F*) Scanning electron micrographs show the topography of the surface (*E*) and the inner core (*F*) of a BioCer tile of an experimental implant.

19%) compared with BioCer (center, 63%; periphery, 70%) (Fig. 2*P*).

Backscattered electron-scanning electron microscopy (BSE-SEM) corroborated the histological observation of osteonal bone at the periphery of the Ti and BioCer implants. Ti exhibited more separation from the bone (Fig. 3 *A* and *C*). In contrast, irrespective of the location within the defect (periphery or center), union with bone was observed for the BioCer implant (Fig. 3 *B* and *D*) and verified by high-angle annular dark-field scanning transmission electron microscopy (HAADF-STEM) and energy-dispersive X-ray spectroscopy (EDS) (Fig. 3 *E* and *F*).

Mineral crystallinity of bone formed centrally in the BioCer and peripherally in the Ti was higher than that of the native bone (Fig. 3*G*). Carbonate-to-phosphate (Fig. 3*H*) and apatite-to-collagen (Fig. 3*I*) ratios were higher in the native bone, indicating more aged tissue. The higher carbonate-to-phosphate ratio for BioCer (vs. Ti) at the periphery indicated more mature tissue (Fig. 3*H*).

Detailed results are provided in *SI Appendix*, Results 1.1.

Ectopic Bone Formation at Subcutaneous Sites. After 3 mo, no adverse reactions to the BioCer or Ti implants were observed macroscopically (Fig. 4 *A* and *B*). Histological analysis demonstrated ectopic bone formation at subcutaneous (s.c.) sites of BioCer implants (Fig. 4 *D*, *G*, *H*, *J*, and *K*) but not Ti implants (Fig. 4*C*). Bone was detected on the surface and in the concavities of the partially degraded material. This bone had the characteristics of newly formed bone, albeit with a lamellar structure (plexiform). Osteocytes, osteoblast seams, and blood vessels were frequently detected. Large multinucleated cells were often observed on the BioCer surface (Fig. 4 *I* and *L*). The multinucleated cells appeared to participate in material degradation, as they were associated with eroded surfaces and exhibited phagocytosis of BioCer particulates.

The overall scores revealed bone in all animals (six of six) with BioCer implants, whereas bone was never detected in animals with Ti implants (0 of six) (Fig. 4 *E* and *F*). Bone was more frequently detected in the central third than in the third facing the skin (Fig. 4*F*).

BSE-SEM confirmed ectopically formed lamellar bone, with osteocyte lacunae aligned parallel to the BioCer surface (Fig. 5 *A*–*C*). Raman spectroscopy of the ectopic bone revealed organic and inorganic components typical of bone, including carbonated apatite and collagen (Fig. 5*D*).

Clinical Retrieval. Bone formation and the bridging of tiles were indicated by computed tomography (CT) prior to explantation. Macroscopically, the BioCer implant was integrated with well-vascularized bone and soft tissues at explantation (Fig. 6 *A* and *B*).

Histologically, the implant components (BioCer tiles and Ti frame) showed integration with the surrounding tissue and bone, with no signs of adverse reactions (Fig. 6 *C*–*K*). A considerable amount of mature, vascularized, osteonal bone was found in association with the BioCer tiles, including in the most central zone of the implant. Bone enveloped the tiles and bridged the intertile spaces.

The smallest amount of bone was found in conjunction with the exposed Ti in the transitional zone (Fig. 6*E*). Bone formation and integration were found in relation to the Ti mesh elsewhere (Fig. 6 *C*, *D*, *F*, and *G*). With BioCer, bone formation–resorption coupling occurred within porosities and concavities (Fig. 6*I*). As observed in the sheep skull, the periosteum and endosteum were restored on the skin and dura sides of the BioCer (Fig. 6 *J* and *K*).

For both tile and intertile ROIs (Fig. 7 *A* and *B*), the central zone of the implant revealed a larger bone area than the transitional zone (Fig. 7 *C* and *E*). High BioCer–bone contact was demonstrated in the tile (78 to 91%) (Fig. 7*D*) and intertile (88%) (Fig. 7*F*) ROIs. In the intertile ROI of the transitional zone, the Ti exhibited lower bone contact (2%) than the BioCer (88%) or the Ti frame in the peripheral (78%) and central (65%) zones (Fig. 7*F*).

Bone growth into the intertile ROI (indicative of bridging between tiles) revealed the highest values in the central zone (80%) (Fig. 7*G*). The observation of tile bridging and a larger amount of bone in the peripheral and central zones than in the transitional zone was further supported by micro-CT (Fig. 7 *I*–*K*).

As determined using Raman spectroscopy, the composition of the regenerated bone was typical of mature lamellar bone and similar to that of the control, native bone (Fig. 8 *A*–*D*).

HAADF-STEM imaging and EDS demonstrated ultrastructural and chemical bonding between the BioCer and the human cranial bone (Fig. 8 *E* and *F*).

Compositional Fingerprint of Regenerated Bone and Transformation of the BioCer Implants In Vivo. The Raman spectroscopy results for regenerated bone are summarized in Fig. 9*A*. In the human skull,

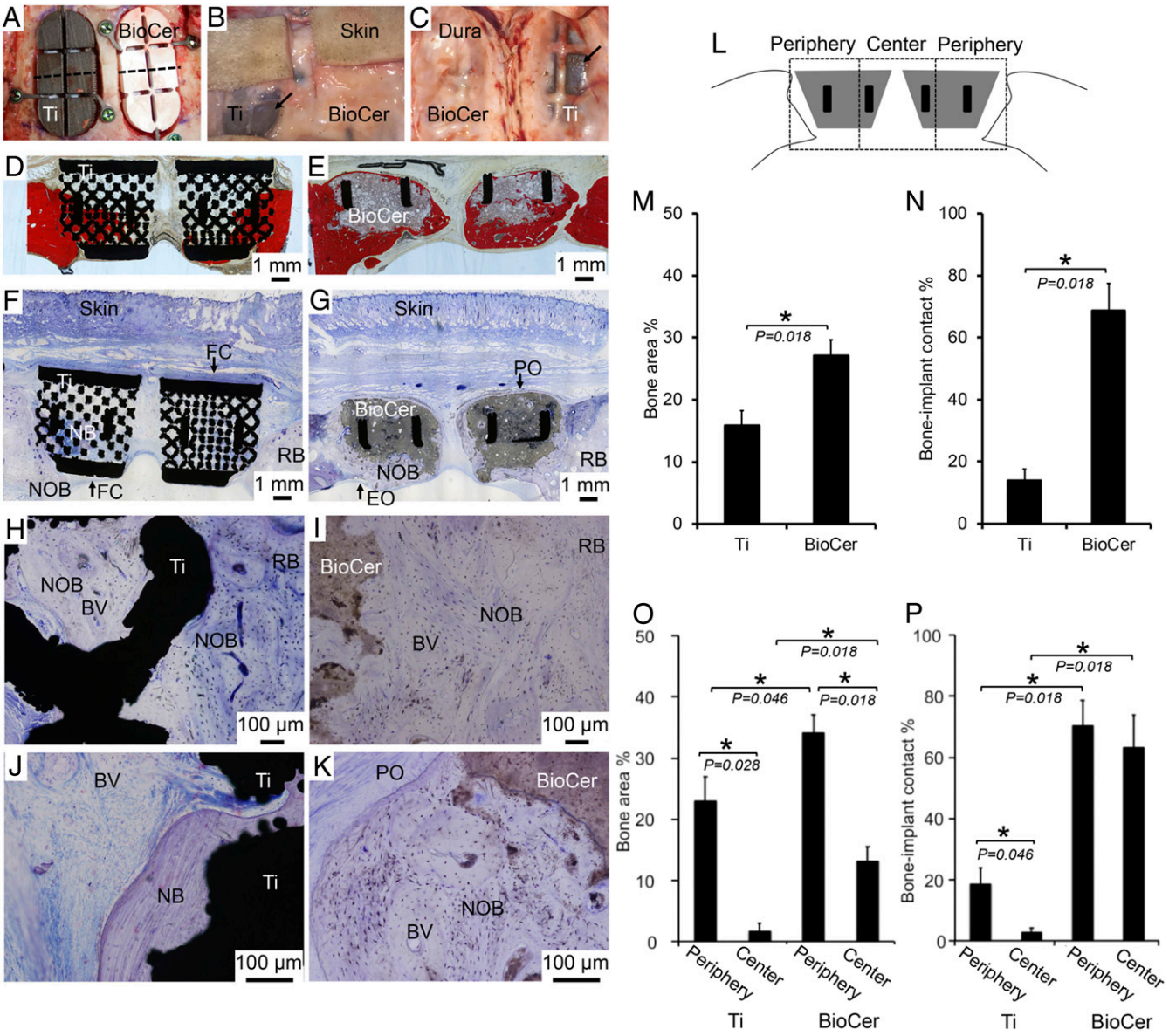

Fig. 2. Sheep skull implantation and investigations after 12 mo (histology and histomorphometry). (*A*) Parietal bone defects were treated with either a bioceramic (BioCer) or titanium (Ti) implant. The dotted lines in *A* indicate the site of histological sections after retrieval. After 12 mo, the BioCer appeared to be well integrated on both the skin (*B*) and dura (*C*) sides, whereas for Ti, partial soft tissue coverage and a visible metal surface (black arrows) were observed on the skin and dura sides. (*D* and *E*) Survey cross-sections (van Gieson's stain) corresponding to the black dotted lines in *A*. (*A*–*K*) Micrographs of toluidine blue-stained sections showing the pattern of bone formation for the Ti (*F*, *H*, and *J*) and BioCer (*G*, *I*, and *K*) implants. The Ti shows new osteonal bone (NOB) with central blood vessels (BVs) mainly as ingrowth from the native recipient bone (RB) (as shown in *F* and *H*), whereas the new bone (NB) formed in the center of the Ti implant does not reveal a well-remodeled structure (as shown in *J*). With the BioCer, there is a considerable amount of NOB, with central BV filling the different regions of the defect, as exemplified in the peripheral (*I*) and central (*K*) regions. The skin and dura sides of the Ti are covered with a thick fibrous capsule (FC), whereas the BioCer shows the formation of periosteum (PO) and endosteum (EO) on the skin and dura sides, respectively. Histomorphometric analyses of the different ROIs (*L*) in the defect demonstrate a significantly larger bone area (*M* and *O*) and higher bone–implant contact (*N* and *P*) for the BioCer than for the Ti, both at the total defect area level (*M* and *N*) and in the peripheral and central ROIs (*O* and *P*). Statistical comparisons were performed using paired Friedman and Wilcoxon signed-rank tests.

bone formed at the center and periphery of the BioCer implant was compositionally similar to native bone. In the sheep skull, the carbonate-to-phosphate and mineral-to-matrix ratios of the native bone were higher than those of newly formed bone (after 12 mo) adjacent to the peripheral regions of the Ti and BioCer implants and the central region of the BioCer implants. In the sheep soft tissue, the newly formed bone (after 3 mo) adjacent to the central region of the BioCer implants was compositionally similar to well-mineralized, native bone.

Raman spectroscopy demonstrated BioCer implant transformation in vivo (Fig. 9*B*). The BioCer implants showed varying extents of conversion to carbonated apatite at the expense of monetite, β-CPP, and β-TCP at the three analyzed locations (near Ti, bulk, and near bone). The strongest conversion to apatite tended to occur within 10 to 100 µm of the bone–implant interface (i.e., near bone). This conversion was most advanced in the sheep soft tissue and least advanced in the sheep skull, where monetite remains detectable. In the "near Ti" and "bulk" areas, the ceramic retained varying amounts of TCP and calcium pyrophosphate. Corroborating the Raman findings, XRD and quantitative analysis using Rietveld refinement (*SI Appendix*, Fig. S30) on human samples revealed in vivo phase transformation to apatite

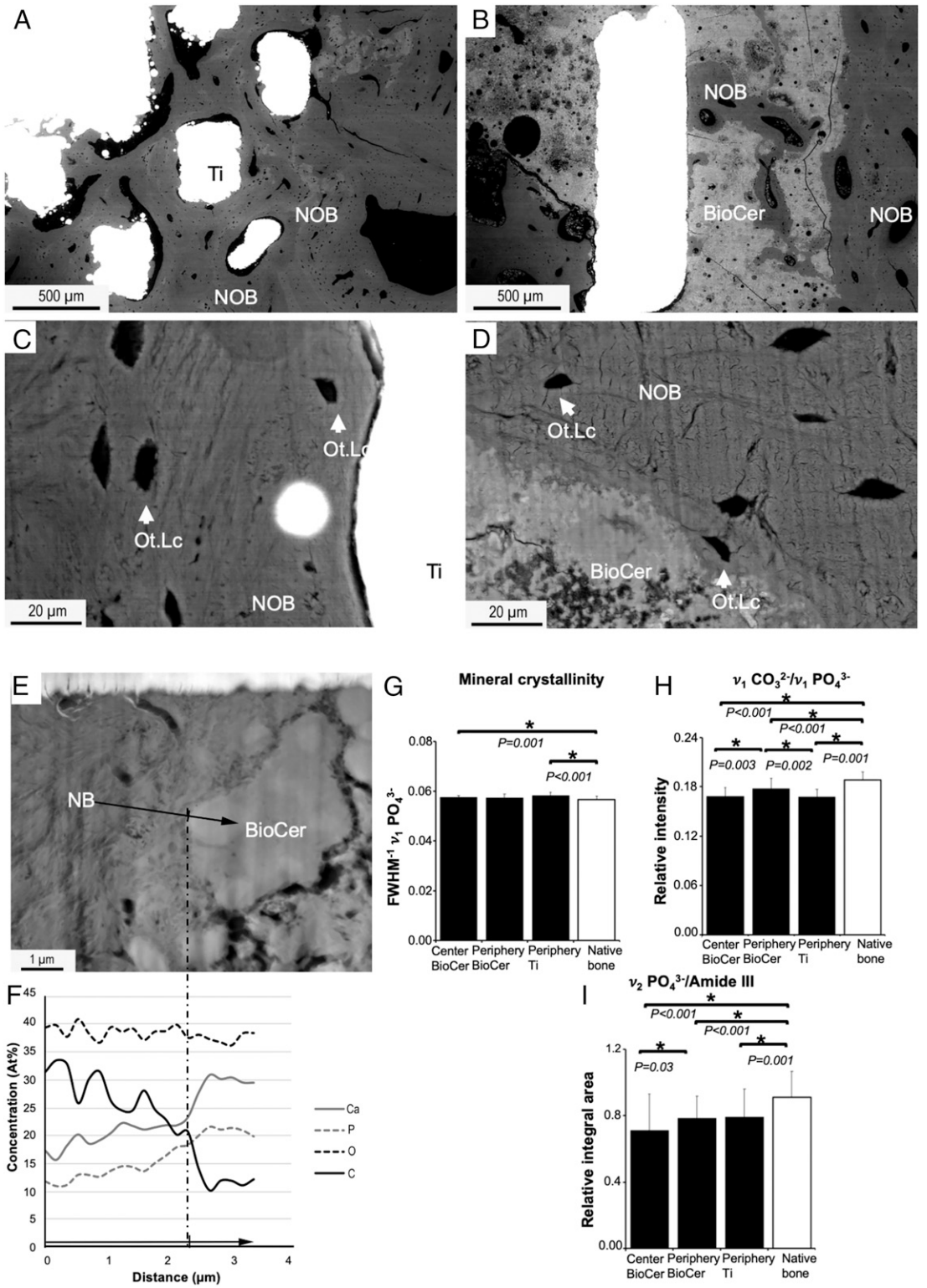

Fig. 3. Sheep skull implantation and investigations after 12 mo (ultrastructure and composition). The backscattered electron-scanning electron microscopy (BSE-SEM) micrographs show the new osteonal bone (NOB) in the peripheral regions of the titanium (Ti) (*A* and *C*) and bioceramic (BioCer) (*B* and *D*); separation is commonly detected between NOB and the surface of Ti, whereas NOB is found in direct contact with the BioCer. Osteocyte lacunae (Ot.Lc) are commonly encountered in the vicinity of both the Ti and BioCer surfaces (exemplified by white arrows in *C* and *D*). (*E*) High-angle annular dark-field scanning transmission electron microscopy (HAADF-STEM) image showing the ultrastructural union between the new bone (NB) and the BioCer surface. (*F*) Elemental analysis, using energy-dispersive X-ray spectroscopy (EDS), across the interface reveals the continuity of the calcium (Ca), phosphate (P), oxygen (O), and carbon (C) signals from the NB into the BioCer, along the black arrow in *E*. Although higher Ca and P ion concentrations are observed in BioCer, the Ca/P ratio is comparable for BioCer and NB. (*G–I*) Raman spectroscopy. The mineral crystallinity ($FWHM^{-1}$ ν_1 PO_4^{3-}; *G*) in the center of BioCer and the periphery of Ti is higher than that in the native sheep skull bone. The bone in the periphery of BioCer shows mineral crystallinity similar to that of the native bone. The carbonate-to-phosphate ratio (ν_1 CO_3^{2-}/ν_1 PO_4^{3-}; *H*) and the apatite-to-collagen ratio (ν_2 PO_4^{3-}/amide III; *I*) are higher in the native bone than in the NB formed in the Ti- or BioCer-treated defects. The statistical comparisons were performed using nonpaired Kruskal–Wallis and Mann–Whitney *U* tests.

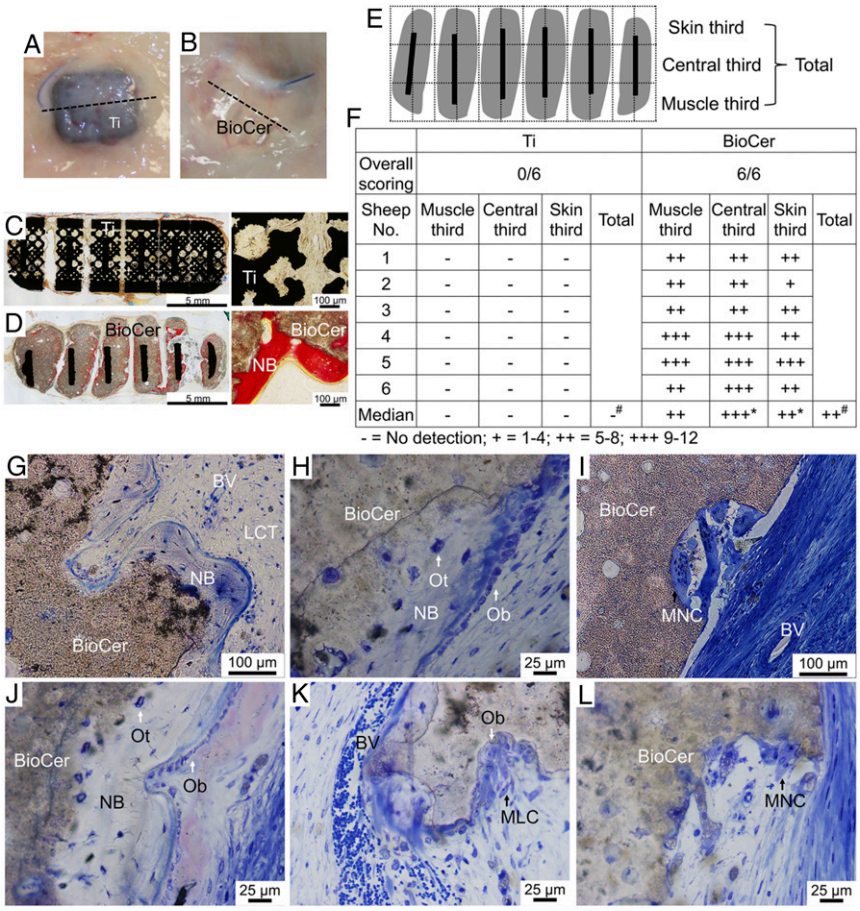

Fig. 4. Sheep dorsal s.c. investigations after 3 mo of implantation (histology). (*A* and *B*) No adverse soft tissue responses are observed macroscopically for titanium (Ti) or bioceramic (BioCer). The dotted lines in *A* and *B* indicate the site of histological sectioning. (*C* and *D*) The survey light micrographs (van Gieson's stain) show the two implant types (Ti and BioCer), each consisting of six tiles and five slits, interfacing with the s.c. tissue toward the skin (*Top*) and muscle (*Bottom*) sides. New bone (NB) (red staining) is detected with BioCer (as exemplified in *D*) but not Ti (as exemplified in *C*). The prevalence of bone in different ROIs was determined histologically using a software grid (*E*), with data presented in the table (*F*). The scoring was recorded as follows: –, no bone detected in any of the 12 rectangles; +, bone detected in 1–4 out of 12 rectangles; ++, bone detected in 5–8 out of 12 rectangles; and +++, bone detected in 9–12 out of 12 rectangles. Statistically significant differences are indicated by a hash sign ($P = 0.027$; $n = 6$) and asterisk ($P = 0.042$; $n = 6$). The comparisons were performed using paired Friedman and Wilcoxon signed-rank tests. (*G*–*L*) Light micrographs of toluidine blue-stained sections show the formation of ectopic NB in the BioCer implant. The NB is formed directly on the BioCer surface, with the typical appearance of osteoblasts (Ob), depositing a layer of darkly stained osteoid, and osteocytes (Ot) embedded in the NB (some of the osteoblasts and osteocytes are indicated by white arrows). Loose connective tissue (LCT) with blood vessels (BVs) is found in the close vicinity of the ectopic NB. Multinucleated cells (MNCs) are frequently encountered in association with concavities in the BioCer surface. Some of the MNCs appear to contain material particulates (black arrow in *L*). In other regions, the concavities in the resorbed BioCer surface are occupied by osteoblasts (Ob) depositing NB in close proximity to mesenchymal-like stem cells (MLCs) and BVs (as exemplified in *K*).

(calcium-deficient HA, 69.5 ± 3.9%) and TCP (Mg-substituted TCP, 15 ± 4.9%; β-TCP, 6.3 ± 1.2%) at the loss of β–CPP (6.5 ± 3.4%) and monetite (2.6 ± 1.2%) (*SI Appendix*, Fig. S30*B* and Table S2).

Additional results are provided in *SI Appendix*.

Discussion

This study explored the hypothesis that an implant design consisting of a mechanically robust scaffold with a BioCer coating and well-defined macroporosity would enable primary stability, bone ingrowth, and osseointegration, together with adaptation to the dura mater and the overlying skin, without causing adverse responses.

In the sheep skull, the BioCer implant promoted a higher degree of bone formation, remodeling, and osseointegration, leading to enhanced repair of the cranial defect in comparison to the Ti implant. Moreover, endosteal and periosteal regeneration were evident in the morphological analyses. A partial, albeit indirect, explanation of the superior performance of the BioCer implant in cranial defects was provided by assessment of the implanted BioCer and Ti materials in soft tissues. Only BioCer promoted bone formation and maintained bone outside the skeletal envelope for 3 mo. Interestingly, the induced bone had morphological, ultrastructural, and chemical characteristics similar to those of the native skull bone and the bone regenerated in the skull defects.

Considering the clinical translation of customized cranial implants, the structural integrity and regenerative potential of the tissue at the recipient site could differ markedly from those observed under controlled, experimental conditions. Nevertheless, the experimental observations were corroborated by analysis of an entire implant retrieved from a patient 21 mo postoperatively. Histological, ultrastructural, and compositional analyses demonstrated the regeneration of mature, remodeled, and vascularized bone. Interestingly, the regenerated bone associated with the BioCer implant had a composition similar to that of the native bone, regardless of the location within the defect.

Several factors, including mechanical factors (36, 37), the properties of implanted biomaterials (38), and the available biological

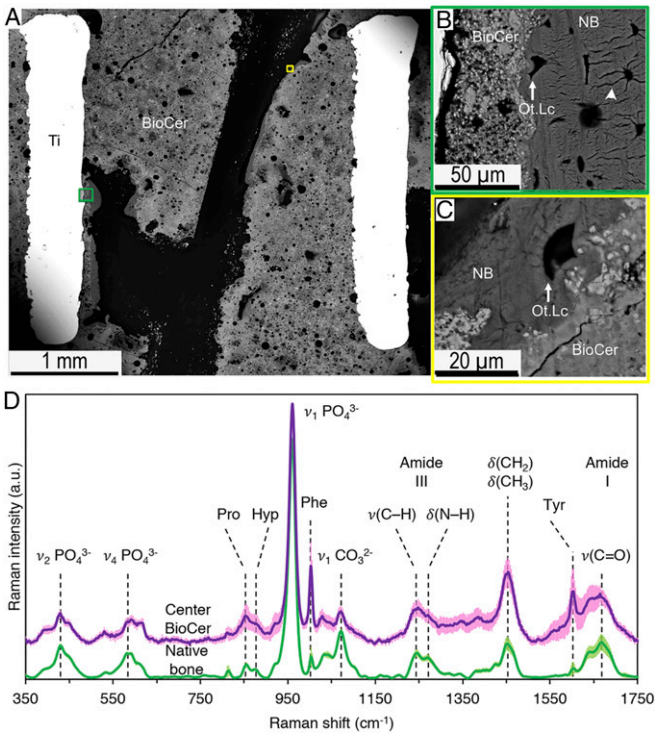

Fig. 5. Sheep dorsal s.c. investigations after 3 mo of implantation (ultrastructure and composition). (*A*) Backscattered electron-scanning electron microscopy (BSE-SEM) of bioceramic (BioCer) implants in s.c. sites. The green and yellow *Insets* in *A* are presented at a higher magnification (*B* and *C*, respectively). (*B* and *C*) Ectopic new bone (NB) on the BioCer in the central zone of the implant. Several osteocyte lacunae (Ot.Lc; white arrows in *B* and *C*) and canaliculi (white arrowhead in *B*) are detected in the NB. (*D*) Averaged Raman spectra of ectopic NB in the BioCer (purple) show an extracellular matrix composition similar to native bone (green). For both, the main phosphate peak (ν_1 PO_4^{3-}; 960 cm^{-1}) is sharp and symmetrical. Bands representing type I collagen, i.e., amides I and III, are evident. Furthermore, amino acids, including proline (Pro; 850 cm^{-1}), hydroxyproline (Hyp; 880 cm^{-1}), phenylalanine (Phe; 1,003 cm^{-1}), and tyrosine (Tyr; 1,600 cm^{-1}), are also detected. The comparatively lower carbonate content (CO_3^{2-}; 1,070 cm^{-1}) of the ectopic bone is attributable to the relative tissue age.

cues [dura mater (39), stem cells (8, 40), and growth factors (10)], have been implicated in the regeneration of bone within large defects. Bone formation occurs mainly from the existing borders of the bone and to a lesser degree in the defect center (36). On the other hand, it has been shown experimentally that dura mater stem cells (39), as well as administered adipose-derived adult stromal cells (8, 40) and growth factors (10, 11), promote bone regeneration in cranial defects. Temporal observations of the involved biological processes using a combination of morphological and molecular techniques are therefore warranted to determine the precise cellular and molecular mechanisms.

Current treatments for cranial defects employ autologous bone grafts and an array of different alloplastic materials (41–43). Ti is a chemically stable, mechanically adequate material that has appropriate biocompatibility in many types of tissue. By virtue of their ability to integrate with bone (osseointegration), the majority of implants used in oro-maxillo-facial reconstruction are manufactured from commercially pure Ti or its alloys (44). The 3D-printed Ti scaffolds, particularly those exhibiting reduced stiffness, promote bone regeneration in large segmental defects in load-bearing long bones (45). Consistently, Ti is considered a suitable material for the mesh of cranial implants (43), providing mechanical support for biological processes that should ultimately lead to bone regeneration in the cranial defect. Interestingly, the excellent biological and clinical results of Ti in oral (25, 46) and orthopedic (47) applications were surpassed by those of the BioCer implant in cranial defects. Here, considerably less bone formation and osseointegration was revealed in the transitional zone for the exposed Ti (2%) than for the BioCer (88%). A similar observation was made in the experimental skull defect. These observations indicate that Ti alone is not sufficient to elicit an appropriate biological response and restore large, cranial defects.

Interestingly, the highest degree of bone regeneration and osseointegration was observed in the central region of the BioCer implant, distant from native bone. An understanding of the role of the implant design and composition in the promotion and maintenance of bone is therefore of crucial importance. The BioCer composition with monetite, β-TCP, and calcium pyrophosphate

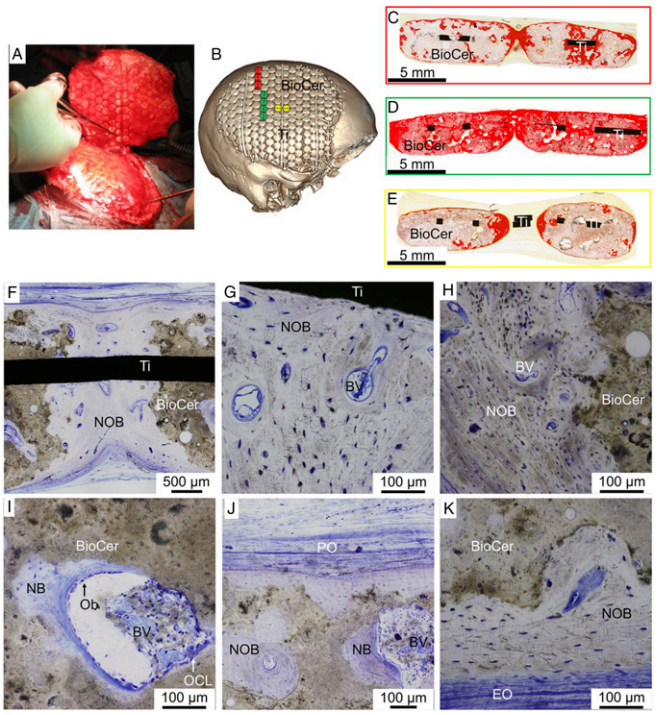

Fig. 6. Investigations of clinical implant retrieved from the human skull after 21 mo (histology). (*A*) Photograph showing the surgical flap dissection and elevation to uncover the bioceramic (BioCer) implant for retrieval. (*B*) A CT scan conducted prior to implant retrieval shows the implant in the recipient skull after 21 mo. The customized implant consists of a laser-cut titanium (Ti) frame enveloped by multiple interconnected hexagonal BioCer tiles. The joint [indicated by (Ti) in *B*] between two adjacent Ti meshes (transitional zone) is not covered by BioCer and has a relatively larger intertile space. The red-, green-, and yellow-coded tiles in *B* are examples of the peripheral, central, and transitional zones that were subsequently processed and analyzed (the full details are provided in *SI Appendix*, Fig. S16). (*C–E*) Survey micrographs (van Gieson's stain) corresponding to the peripheral (red), central (green), and transitional (yellow) zones in *B*, respectively. (*F–K*) Selected micrographs of toluidine blue-stained sections of central and peripheral tile and intertile regions of the BioCer. (*F*) Survey micrograph showing complete bridging of an intertile space by well-vascularized, new osteonal bone (NOB) in a central zone, integrating the BioCer as well as the Ti. (*G*) A higher-magnification image of NOB, with blood vessels (BVs), formed within a BioCer tile in a central zone, interfacing with the Ti within the BioCer. (*H*) An intertile region in a peripheral zone, where NOB with central BVs is visible. (*I*) Areas with resorption of the BioCer reveal a typical bone-remodeling pattern, with osteoclast-like cells (OCL) (white arrow) concomitant with an osteoblast (Ob) seam (black arrow), new bone (NB), and BVs. (*J* and *K*) Vascularized NOB on the skin (*J*) and dura (*K*) sides of a tile in the central zone. Periosteum (PO) and endosteum (EO) cover the NOB.

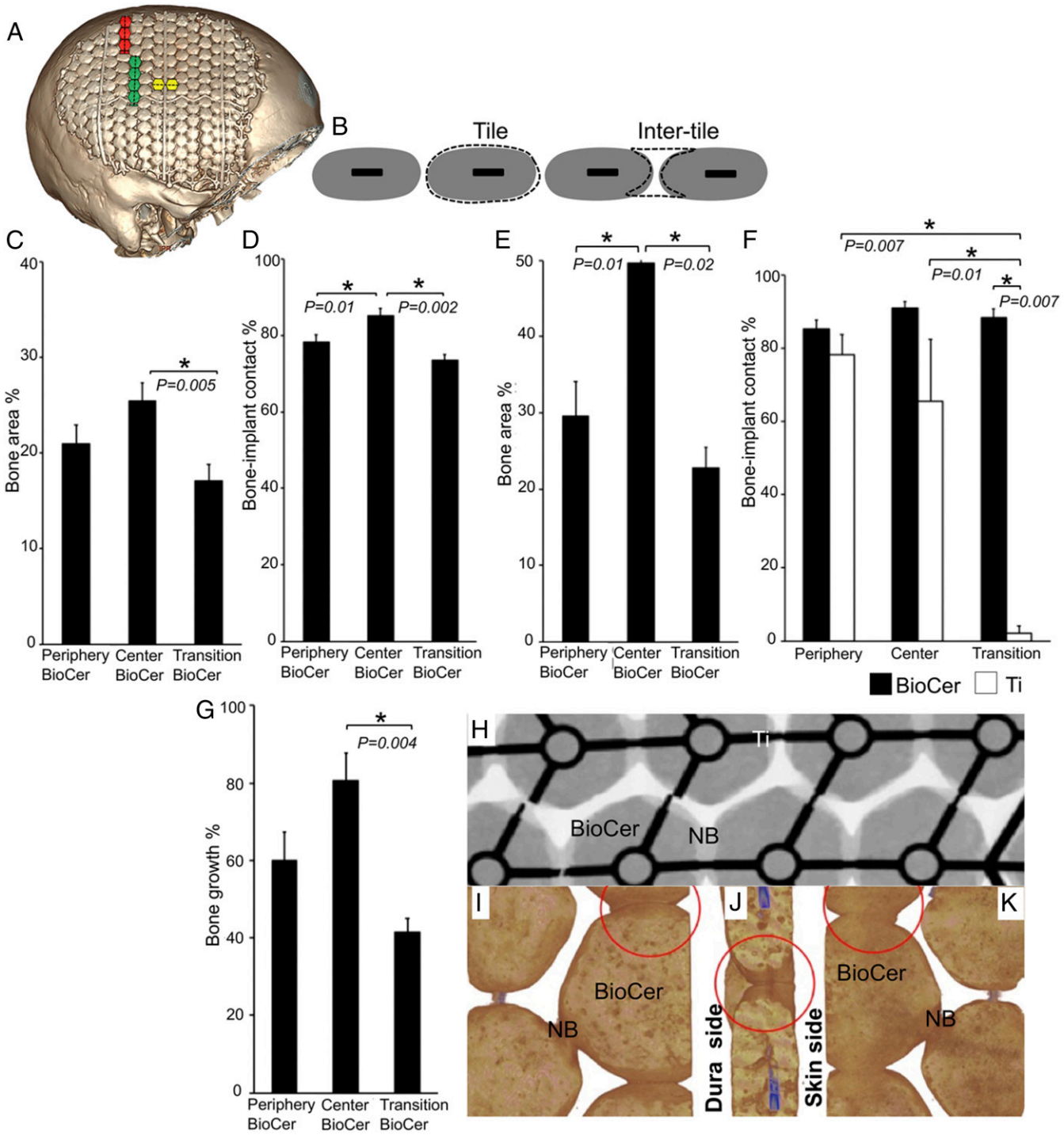

Fig. 7. Investigations of clinical implant retrieved from the human skull after 21 mo (histomorphometry). (*A*) A CT scan shows the implant in the recipient skull. The red-, green-, and yellow-coded tiles in *A* are examples of peripheral, central, and transitional zones that were subsequently processed and analyzed. (*B*) Schematic of the tile and intertile regions of interest (ROIs) used for histomorphometry. (*C* and *D*) In the tile ROI, the largest bone area (*C*) and bone–implant contact (*D*) are detected in the central zone of the implant, whereas the lowest values are found in the transitional zone. (*E*–*G*) In the intertile ROI, the largest bone area (*E*) and bone growth distance (*G*) are detected in the central zone, and the smallest bone area and bone growth distance are found in the transitional zone. In *F*, significantly less bone contact is found for the exposed titanium (Ti) than for the bioceramic (BioCer) in the transitional zone or the Ti in the peripheral and central zones. The statistical comparisons were performed using nonpaired Kruskal–Wallis and Mann–Whitney *U* tests. (*H*) The 2D microcomputed tomography (micro-CT) image in the central zone shows the new bone (NB), in light gray contrast, bridging adjacent tiles of the BioCer (darker gray contrast), as well as integrating the Ti. Complete bridging with NB is also found between several adjacent tiles in the 3D micro-CT images of the dura (*I*) and skin (*K*) sides (represented by the circles in *I* and *K*). The dura side *K* has a rougher appearance, indicating less bone coverage than observed on the skin side, which has a smoother appearance (*I*). More NB filling on the skin side than on the dura side was confirmed in a cross-sectional micro-CT image (*J*).

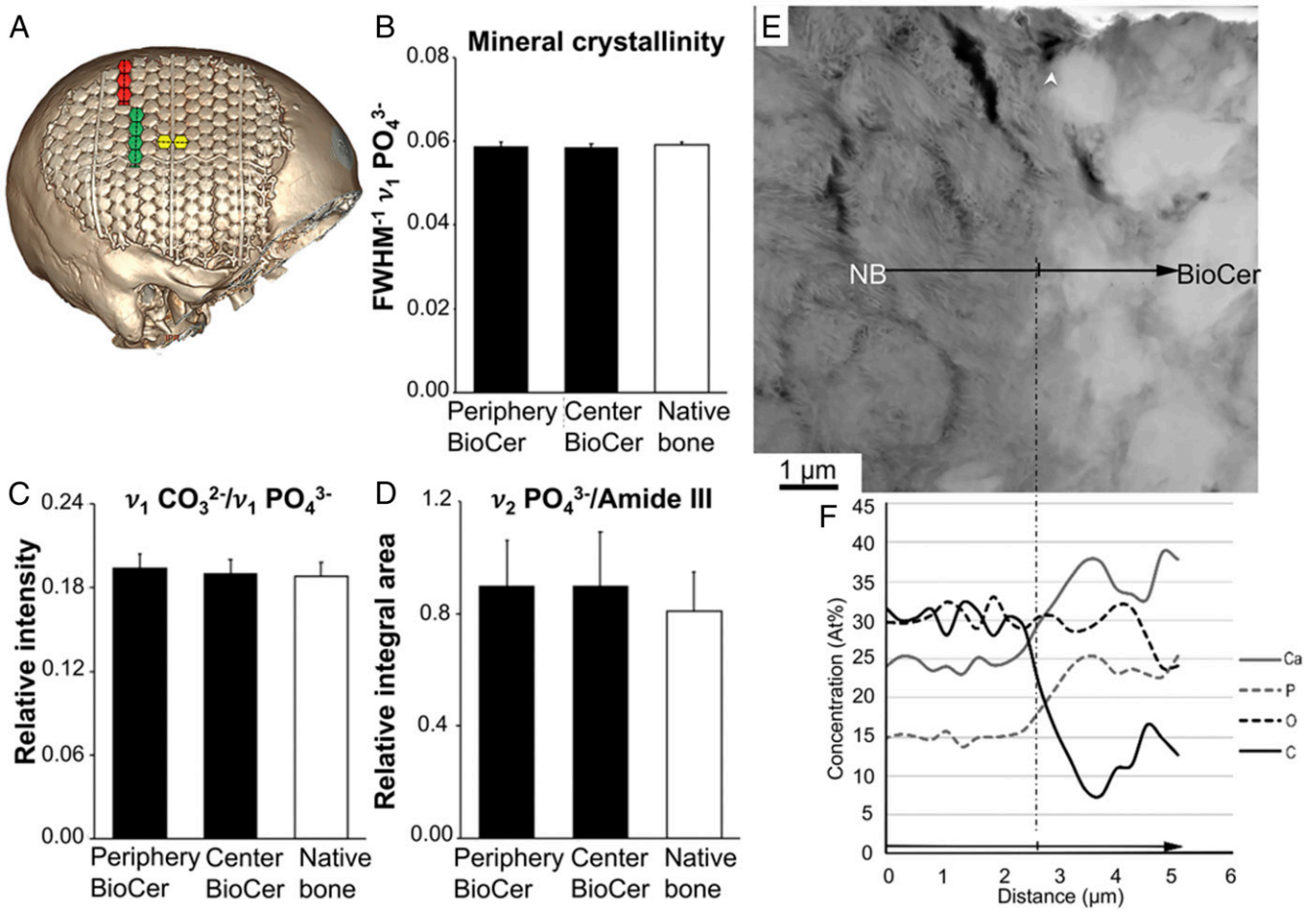

Fig. 8. Investigations of clinical implant retrieved from the human skull after 21 mo (ultrastructure and composition). (*A*) A CT scan shows the implant in the recipient skull. The red-, green-, and yellow-coded tiles in *A* are examples of the peripheral, central, and transitional zones that were processed and analyzed. (*B–D*) Raman spectroscopy. (*B*) The mineral crystallinity (FWHM^{-1} ν_1 PO_4^{3-}), (*C*) the carbonate-to-phosphate ratio (ν_1 CO_3^{2-}/ν_1 PO_4^{3-}), and (*D*) the apatite-to-collagen ratio (ν_2 PO_4^{3-}/amide III) of peripheral and central intertile bone in the bioceramic (BioCer) implant are similar to those of the native bone (biopsy from the recipient skull). (*E*) High-angle annular dark-field scanning transmission electron microscopy (HAADF-STEM) image shows the union of new bone (NB) with the BioCer surface. (*F*) Elemental analysis, using energy-dispersive X-ray spectroscopy (EDS), across the interface reveals the continuity of Ca, P, O, and C signals from the NB into the BioCer, along the black arrow in *E*, with higher contents of calcium and phosphorus in the BioCer and a higher content of carbon in the bone.

differs from that of other cranial implants made of calcium phosphates that have been introduced clinically (48). Some support for osteogenic differentiation associated with bone formation around the BioCer implant in vivo in both the central and peripheral regions of the cranial defect was provided in a case study (49). One possible mechanism, proposed by Ripamonti et al. (50), involves the microarchitecture (e.g., repetitive concavities, simulating the basic multicellular unit) of the material surface exposed to the biological surroundings. As shown here, these microenvironments may be created during the slow degradation of BioCer when pores (i.e., concavities) are exposed to surrounding cells and fluids. Cells (e.g., macrophages and osteoclasts) may actively condition the surface of the BioCer, thereby creating a topology that enables active bone formation and subsequent remodeling. This assumption is supported by the present observations of osteoclasts, osteoprogenitors, and osteoblasts at the BioCer surface in conjunction with the formation of well-vascularized bone.

A major finding in the present study is that the implant, consisting of a 3D-printed titanium frame enveloped within a BioCer consisting of three different CaP phases, was able to induce bone regeneration, at both skeletal and nonskeletal sites. Despite extensive research, the exact mechanism of material-induced ectopic bone formation is still unknown, although several theories have been proposed. For instance, it has been suggested that the release of Ca and P ions and the adsorption of pro-osteogenic growth factors and cytokines stimulate inflammatory and regenerative cells (51). Furthermore, it has been proposed that the process of CaP dissolution–reprecipitation on the material surface, particularly within the micropores, may play a significant role in ectopic bone formation (52). The major physical, chemical, and biological factors involved in material-associated osteoinduction were the subject of a recent review discussing a new potential mechanism of osteoinduction: Local depletion of Ca^{2+} and PO_4^{3-} caused by apatite precipitation on the material surface can trigger a relevant biological response (23). In addition, material transformation of less stable/metastable CaP precursors to bone-resembling apatite phases has also been implicated in the osteoinductive properties of CaP (53). The present studies show that the BioCer implant in fact undergo such transformation to apatite. Importantly, the XRD and Raman spectroscopy analysis of nonimplanted (native) as well as retrieved implant from human skull show that this transformation occurs in vivo, after long-term implantation, and not due to material processing before implantation.

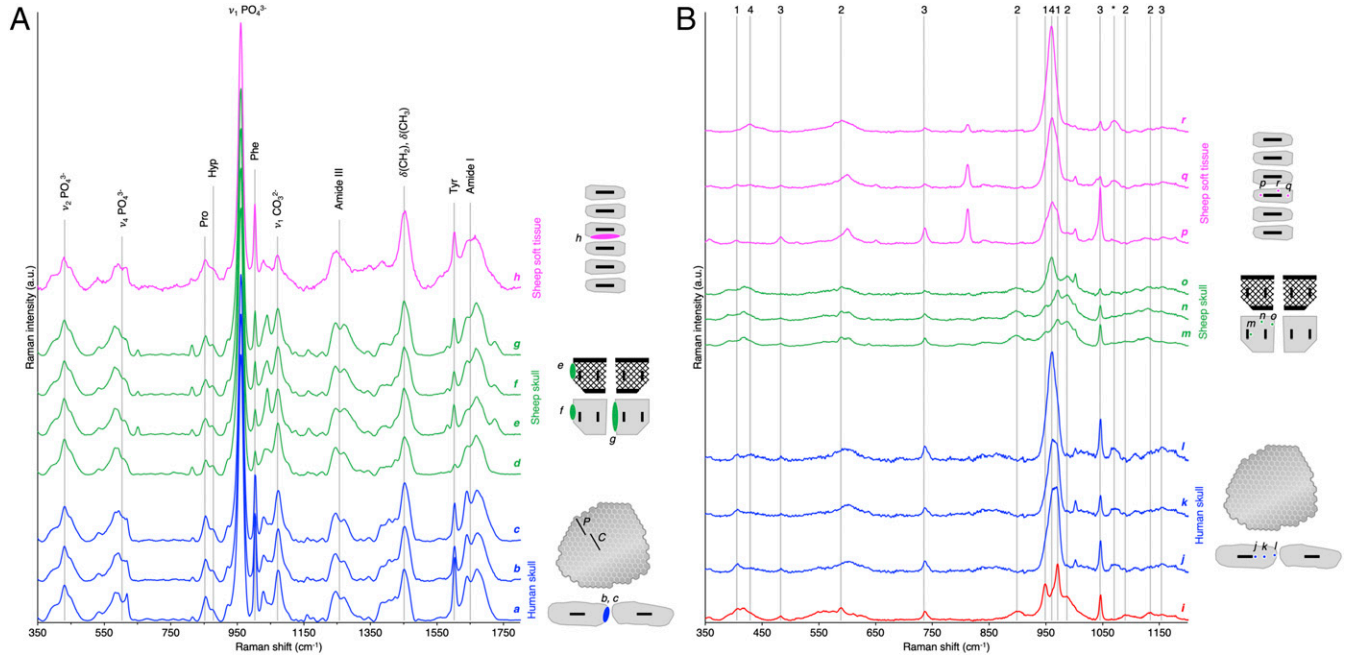

Fig. 9. Raman spectroscopy characterization of the regenerated bone and material transformation. (*A*) Raman measurements of the native skull bone and bone regenerated in peripheral, P, and central, C, regions of titanium (Ti) and bioceramic (BioCer) implants in the human skull, sheep skull, and sheep s.c. soft tissue. Labels *a*–*h* indicate the various regions analyzed in bone: native bone (*a*, *d*), periphery of BioCer (*b*, *f*), periphery of Ti (e), and center of BioCer (*c*, *g*, *h*). (*B*) Raman measurements of the bioceramic (BioCer) implant prior to implantation and after retrieval from the human skull, sheep skull, and sheep s.c. soft tissue. Labels 1 to 4 indicate spectral features characteristic of the various calcium phosphate phases detected: 1, β-tricalcium phosphate (β-TCP); 2, dicalcium phosphate anhydrous (monetite); 3, dicalcium pyrophosphate (β-CPP); 4, carbonated apatite; *, v_1 CO_3^{2-}. Raman spectra of the BioCer were collected adjacent to the titanium frame ("near Ti"), in the middle of the BioCer tile ("bulk"), and 10 to 100 μm from the bone–implant interface ("near bone"). Labels *i*–*r* indicate the various regions analyzed in the BioCer: native nonimplanted BioCer (*i*), near Ti (*j*, *m*, *p*), bulk (*k*, *n*, *q*), and near bone (*l*, *o*, *r*). The illustrations show the specific regions where the analysis was performed.

Therefore, detailed studies on the apatite transformation processes and their kinetics in vivo are warranted.

Mechanical protection of the brain is a critical role of cranial implants. A limitation of the present study is the absence of a mechanical evaluation after bone regeneration and integration with the surrounding tissue. Previous studies have shown appropriate mechanical properties of the present material in comparison with native skull (54). Furthermore, the cranial implant, consisting of BioCer tiles interconnected by an additively manufactured grade 23 Ti frame, equivalent to the present experimental BioCer implant, provided the best match for the stiffness of the skull in comparison with commercial implants made of PEEK and Ti (54). Another limitation is that the study did not include cellular and molecular techniques, such as immunohistochemistry and gene expression analysis, to shed light on the underlying mechanisms of the transition from empty space to considerable bone repair, without the application of exogenous cells and growth factors. Here, a detailed analysis of the early events involved in the recruitment of different cell types and their subsequent stages of differentiation in vivo is particularly important. This requires kinetic studies of the different cells (macrophages, osteoblasts, and osteoclasts) and their expression and secretion of factors implicated in bone healing, regeneration, and remodeling.

The results of the experimental and clinical retrieval studies provide proof-of-concept that this BioCer implant design and composition promote in situ bone regeneration and osseointegration. The design and material composition created a local environment conducive to in situ bone regeneration at both osseous and nonosseous sites, without the administration of exogenous growth factors and cells.

Materials and Methods

A complete description of the materials and methods, including detailed information on the study design and statistical analysis, is given in *SI Appendix*, 2 Materials and Methods.

Study Design. This study investigated whether critical-size cranial bone defects can be regenerated using 3D-printed cranial implants consisting of a Ti-reinforced BioCer without systemic or local application of cells or administration of growth factors. The study design consisted of three parts. In the first part, two large cranial defects (30 × 15 mm) were established in the parietal bone of seven sheep, and in each sheep, one defect received an experimental BioCer implant (test), whereas the other defect received a Ti implant (control). In the second part, BioCer (test) and Ti (control) implants were implanted s.c. in another group of six sheep. Skeletal (skull) and nonskeletal (s.c. tissue) bone regeneration was investigated qualitatively and quantitatively using multiple techniques after 12 and 3 mo, respectively. In the third part, a proof-of-principle that a large hemicraniectomy (13.4 × 11 cm; 115 cm^2) in a human can be restored with new bone, achieving a structure and composition similar to those of normal bone, was provided after detailed investigation of a retrieved, customized BioCer implant 21 mo postsurgery.

Implant Manufacturing.

Experimental implants. The BioCer implant for animal experiments consisted of calcium phosphate tiles reinforced and interconnected by a 3D-printed titanium (Ti) mesh with built-in fixation arms (Fig. 1*A*). The BioCer was prepared from a powder mixture of β-TCP/dicalcium pyrophosphate (Sigma-Aldrich) and monocalcium phosphate monohydrate (Alfa Aesar; Thermo Fisher) and mixed with glycerol (55–57). The BioCer was molded precisely over the Ti frame in the form of rectangular tiles (thickness, 6 mm; spacing, ∼1 mm) and allowed to set overnight in sterile water. After removal from the mold, the implant was left in sterile water for 48 h to eliminate glycerol. The titanium implant (control) (Fig. 1*B*) had a design and dimensions similar to those of the BioCer implant but was entirely additively manufactured

from grade 23 titanium. The dimensions of the implants in the sheep skull and soft tissue experiments were 30 × 15 mm and 18 × 18 mm, respectively. ***Clinical implant.*** The clinically retrieved skull implant consisted of laser-cut Ti, grade 2, covered with mosaic-shaped BioCer tiles with a chemical composition, porosity, density, and surface area identical to those of the experimental BioCer implant. The implant was customized manually to fit a 3D-printed model of the patient defect (Fig. 1*C*) prior to sterilization (OssDsign AB).

All implants, experimental or clinical, were steam sterilized by autoclaving at 121 °C for 20 min.

Material Characterization. After autoclave sterilization, the BioCer material for the experimental and clinical implants was characterized with respect to the following parameters: 1) phase composition, using an X-ray diffractometer (Aeris; Malvern Panalytical Ltd.); 2) porosity, using Archimedes' principle for dry, wet, and immersed weight measurement; 3) specific surface area, using nitrogen adsorption in an ASAP 2020 system (Micromeritics Instrument Company); 4) density, using helium pycnometry in an AccuPyc 1340 pycnometer (Micromeritics Instrument Company); and 5) microstructure, using SEM (Merlin; Zeiss). Furthermore, the amount of glycerol diffusing from the BioCer implant was evaluated with high-performance liquid chromatography–evaporative light scattering detector, using an Agilent 1100 HPLC system and based on exhaustive extraction method.

Animal Surgery. The experiment was approved by the Ministry of National Education, Higher Education and Research (01139.2) (NAMSA, Chasse-sur-Rhône, France) and complied with the ARRIVE guidelines. Seven adult female sheep (*Ovis aries*) underwent skull bone defect implantation. In each sheep, bilateral rectangular defects (15 × 30 mm) were created in the parietal bone. Each defect received either a BioCer or a titanium (Ti) implant. Another group of six adult sheep underwent dorsal s.c. implantation with BioCer and Ti implants in each animal. After 3 mo (s.c. implants) and 12 mo (skull implants), the sheep were killed, and the implants with surrounding tissues were retrieved and fixed in 10% formalin.

Clinical Retrieval. The protocol was approved by the Regional Ethics Committee in Stockholm (Dnr 2017/251031). Retrieval and processing of the implant were performed in accordance with the Biospecimen Reporting for Improved Study Quality guidelines. A 22-y-old male developed a subdural hematoma after a car accident and underwent decompressive hemicraniectomy. Cryopreserved autologous bone was reimplanted after 1.5 mo and explanted 13 mo later due to resorption and a suspected infection. Five months later, the patient underwent cranioplasty with a BioCer implant. The defect size was 13.4 × 11 cm (115 cm^2). Minor trauma caused physical deformation of the implant, necessitating replacement 21 mo postoperatively. The BioCer implant was retrieved and fixed, similar to the experimental implants. The patient provided signed informed consent.

Sample Processing. After fixation, the retrieved clinical and experimental implants were dehydrated, embedded in plastic resin (58), and processed for X-ray micro-CT, histology, histomorphometry, Raman spectroscopy, and electron microscopy.

Analytical Procedures.

Micro-CT. The retrieved clinical implant was scanned and analyzed using a Skyscan 1172 scanner (Bruker micro-CT) and associated computer software. ***Histology and histomorphometry.*** The morphology of the implant-associated tissue and its relationship to the implant in different ROIs was evaluated qualitatively and quantitatively by determining the BA% and BIC% under a light microscope (Nikon Eclipse E600; Nikon NIS-Elements software; Nikon). For the sheep s.c. implants, the prevalence of bone was determined.

Microstructural analysis. The structure of the bone–implant interface was evaluated in resin-embedded and polished half-blocks using low-vacuum SEM (Quanta 200 environmental SEM; FEI Company) operated in BSE mode at an accelerating voltage of 20 kV.

Raman spectroscopy. Using a confocal Raman microscope (WITec alpha300 R) equipped with a 532-nm laser, the composition [mineral crystallinity (59), carbonate-to-phosphate ratio (60), and apatite-to-collagen ratio (61, 62)] of implant-associated bone was evaluated. Interfacial bone in peripheral and central zones of the retrieved clinical implant and the native bone (skull bone biopsy obtained at implant retrieval) were analyzed. In the sheep skull implants, interfacial bone in the peripheral and central regions of the implant and the native bone were analyzed. Interfacial bone in the central region of s.c. BioCer implants was analyzed.

The composition of the BioCer material itself was also analyzed with respect to possible transformation into apatite after implantation. Material analysis was performed before and after implantation using a confocal Raman microscope (Renishaw inVia Qontor) equipped with a 633-nm laser.

Ultrastructural analysis. Selected resin-embedded human and sheep skull implant specimens were used for HAADF-STEM in a Tecnai T20 LaB_6 TEM/STEM (FEI Company). In brief, a focused ion beam (Versa 3D FIB-SEM; FEI Company) was used to prepare electron-transparent (~100 nm thick) samples of the intact bone-BioCer (63). Elemental analysis for calcium (Ca), phosphorus (P), oxygen (O), and carbon (C) was performed using EDS with a nanoprobe in STEM mode.

XRD analysis of the retrieved clinical implant. Retrieved BioCer implant samples ($n = 3$) were harvested from resin-embedded human skull implant, using a trephine, and finely ground in an agate mortar. The samples were analyzed with respect to different crystalline phases using XRD (D8 Advance; Bruker AXS GmbH).

Statistical Analysis. Histomorphometric comparisons of the experimental sheep skull and s.c. implants (BioCer vs. titanium) were analyzed using paired Friedman and Wilcoxon signed-rank tests. Histomorphometric comparisons of the peripheral, central, and transitional zones of the clinically retrieved implant were analyzed using nonpaired Kruskal–Wallis and Mann–Whitney *U* tests. For Raman spectroscopy, nonpaired Kruskal–Wallis and Mann–Whitney *U* tests were used. All statistical analyses were performed in SPSS (v.23; IBM Corporation). All reported *P* values were two sided, and values of $P < 0.05$ were considered statistically significant.

Data and Materials Availability. All data supporting the findings of this study are available within the paper and *SI Appendix*.

ACKNOWLEDGMENTS. We thank Mrs. Lena Emanuelsson and Mrs. Birgitta Norlindh (from the University of Gothenburg, Sweden) for their expertise during the preparation of morphological samples, and Mr. Mathias Lemberger (from the Karolinska Institutet, Sweden) for his assistance during the animal surgery. The study was supported by the BIOMATCELL VINN Excellence Center of Biomaterials and Cell Therapy, the Västra Götaland Region, the Swedish Research Council (Grants 2018-02891 and 2017-04728), the Swedish Foundation for Strategic Research (Grant RMA15-0110), the Swedish state under the agreement between the Swedish government and the county councils, the ALF (Avtal om Läkarutbildning och Forskning) agreement (Grant ALFGBG-725641), the IngaBritt and Arne Lundberg Foundation, the Hjalmar Svensson Foundation, the Adlerbertska Foundation, the Sylvan Foundation, and the Area of Advance Materials of Chalmers and University of Gothenburg Biomaterials within the Strategic Research Area initiative launched by the Swedish government.

1. B. Corliss *et al.*, Complications after in vivo and ex vivo autologous bone flap storage for cranioplasty: A comparative analysis of the literature. *World Neurosurg.* **96**, 510–515 (2016).
2. M. C. Fan *et al.*, Cryopreservation of autologous cranial bone flaps for cranioplasty: A large sample retrospective study. *World Neurosurg.* **109**, e853–e859 (2018).
3. A. Li *et al.*, Cranioplasty complications and costs: A national population-level analysis using the MarketScan Longitudinal Database. *World Neurosurg.* **102**, 209–220 (2017).
4. I. C. Coulter *et al.*, Routine but risky: A multi-centre analysis of the outcomes of cranioplasty in the Northeast of England. *Acta Neurochir. (Wien)* **156**, 1361–1368 (2014).
5. E. Neovius, T. Engstrand, Craniofacial reconstruction with bone and biomaterials: Review over the last 11 years. *J. Plast. Reconstr. Aesthet. Surg.* **63**, 1615–1623 (2010).
6. J. E. Zins, A. Moreira-Gonzalez, F. A. Papay, Use of calcium-based bone cements in the repair of large, full-thickness cranial defects: A caution. *Plast. Reconstr. Surg.* **120**, 1332–1342 (2007).
7. A. N. Renth, M. S. Detamore, Leveraging "raw materials" as building blocks and bioactive signals in regenerative medicine. *Tissue Eng. Part B Rev.* **18**, 341–362 (2012).
8. C. M. Cowan *et al.*, Adipose-derived adult stromal cells heal critical-size mouse calvarial defects. *Nat. Biotechnol.* **22**, 560–567 (2004).
9. J. J. Mao *et al.*, Craniofacial tissue engineering by stem cells. *J. Dent. Res.* **85**, 966–979 (2006).
10. A. C. Docherty-Skogh *et al.*, Bone morphogenetic protein-2 delivered by hyaluronan-based hydrogel induces massive bone formation and healing of cranial defects in minipigs. *Plast. Reconstr. Surg.* **125**, 1383–1392 (2010).
11. Z. S. Patel *et al.*, Dual delivery of an angiogenic and an osteogenic growth factor for bone regeneration in a critical size defect model. *Bone* **43**, 931–940 (2008).
12. T. Thesleff *et al.*, Cranioplasty with adipose-derived stem cells, beta-tricalcium phosphate granules and supporting mesh: Six-year clinical follow-up results. *Stem Cells Transl. Med.* **6**, 1576–1582 (2017).
13. E. Kohan *et al.*, Customized bilaminar resorbable mesh with BMP-2 promotes cranial bone defect healing. *Ann. Plast. Surg.* **74**, 603–608 (2015).
14. O. Omar, I. Elgali, C. Dahlin, P. Thomsen, Barrier membranes: More than the barrier effect? *J. Clin. Periodontol.* **46** (suppl. 21), 103–123 (2019).

15. C. A. Tannoury, H. S. An, Complications with the use of bone morphogenetic protein 2 (BMP-2) in spine surgery. *Spine J.* **14**, 552–559 (2014).
16. A. W. James *et al*., A review of the clinical side effects of bone morphogenetic protein-2. *Tissue Eng. Part B Rev.* **22**, 284–297 (2016).
17. T. Albrektsson, P. I. Brånemark, H. A. Hansson, J. Lindström, Osseointegrated titanium implants. Requirements for ensuring a long-lasting, direct bone-to-implant anchorage in man. *Acta Orthop. Scand.* **52**, 155–170 (1981).
18. P. Branemark, "Introduction to osseointegration" in *Tissue-Integrated Prostheses: Osseointegration in Clinical Dentistry*, P. Branemark, G. A. Zarb, T. Albrektsson, Eds. (Quintessence Publishing Company, Chicago, 1985).
19. J. Roos *et al*., A qualitative and quantitative method for evaluating implant success: A 5-year retrospective analysis of the Brånemark implant. *Int. J. Oral Maxillofac. Implants* **12**, 504–514 (1997).
20. G. Daculsi, B. H. Fellah, T. Miramond, M. Durand, Osteoconduction, osteogenicity, osteoinduction, what are the fundamental properties for a smart bone substitutes. *IRBM* **34**, 346–348 (2013).
21. A. Y. Friedenstein, Induction of bone tissue by transitional epithelium. *Clin. Orthop. Relat. Res.* **59**, 21–37 (1968).
22. R. J. Miron, Y. F. Zhang, Osteoinduction: A review of old concepts with new standards. *J. Dent. Res.* **91**, 736–744 (2012).
23. M. Bohner, R. J. Miron, A proposed mechanism for material-induced heterotopic ossification. *Mater. Today* **22**, 132–141 (2019).
24. M. Esposito, "Titanium for dental applications (I)" in *Titanium in Medicine: Material Science, Surface Science, Engineering, Biological Responses and Medical Applications*, D. M. Brunette, P. Tengvall, M. Textor, P. Thomsen, Eds. (Springer, Berlin, 2001), pp. 827–873.
25. A. Palmquist, O. M. Omar, M. Esposito, J. Lausmaa, P. Thomsen, Titanium oral implants: Surface characteristics, interface biology and clinical outcome. *J. R. Soc. Interface* **7** (suppl. 5), S515–S527 (2010).
26. Z. Sheikh, Y. L. Zhang, F. Tamimi, J. Barralet, Effect of processing conditions of dicalcium phosphate cements on graft resorption and bone formation. *Acta Biomater.* **53**, 526–535 (2017).
27. F. Tamimi, J. Torres, D. Bassett, J. Barralet, E. L. Cabarcos, Resorption of monetite granules in alveolar bone defects in human patients. *Biomaterials* **31**, 2762–2769 (2010).
28. F. Tamimi *et al*., Bone regeneration in rabbit calvaria with novel monetite granules. *J. Biomed. Mater. Res. A* **87**, 980–985 (2008).
29. P. Habibovic *et al*., Osteoconduction and osteoinduction of low-temperature 3D printed bioceramic implants. *Biomaterials* **29**, 944–953 (2008).
30. J. Engstrand, C. Persson, H. Engqvist, The effect of composition on mechanical properties of brushite cements. *J. Mech. Behav. Biomed. Mater.* **29**, 81–90 (2014).
31. A. A. Mirtchi, J. Lemaître, E. Munting, Calcium phosphate cements: Action of setting regulators on the properties of the beta-tricalcium phosphate-monocalcium phosphate cements. *Biomaterials* **10**, 634–638 (1989).
32. Z. Tang *et al*., Comparison of ectopic bone formation process induced by four calcium phosphate ceramics in mice. *Mater. Sci. Eng. C* **70**, 1000–1010 (2017).
33. J. Wang *et al*., Effect of phase composition on protein adsorption and osteoinduction of porous calcium phosphate ceramics in mice. *J. Biomed. Mater. Res. A* **102**, 4234–4243 (2014).
34. D. J. Bonda, S. Manjila, W. R. Selman, D. Dean, The recent revolution in the design and manufacture of cranial implants: Modern advancements and future directions. *Neurosurgery* **77**, 814–824, discussion 824 (2015).
35. D. Tang *et al*., Biofabrication of bone tissue: Approaches, challenges and translation for bone regeneration. *Biomaterials* **83**, 363–382 (2016).
36. C. H. Hämmerle, J. Schmid, N. P. Lang, A. J. Olah, Temporal dynamics of healing in rabbit cranial defects using guided bone regeneration. *J. Oral Maxillofac. Surg.* **53**, 167–174 (1995).
37. A. Roffi *et al*., The role of three-dimensional scaffolds in treating long bone defects: Evidence from preclinical and clinical literature-a systematic review. *BioMed Res. Int.* **2017**, 8074178 (2017).
38. H. Yuan *et al*., Osteoinductive ceramics as a synthetic alternative to autologous bone grafting. *Proc. Natl. Acad. Sci. U.S.A.* **107**, 13614–13619 (2010).
39. C. E. Petrie Aronin *et al*., FTY720 promotes local microvascular network formation and regeneration of cranial bone defects. *Tissue Eng. Part A* **16**, 1801–1809 (2010).
40. B. Levi *et al*., Human adipose derived stromal cells heal critical size mouse calvarial defects. *PLoS One* **5**, e11177 (2010).
41. J. A. Fearon, D. Griner, K. Ditthakasem, M. Herbert, Autogenous bone reconstruction of large secondary skull defects. *Plast. Reconstr. Surg.* **139**, 427–438 (2017).
42. D. A. Harris *et al*., History of synthetic materials in alloplastic cranioplasty. *Neurosurg. Focus* **36**, E20 (2014).
43. U. Spetzger, V. Vougioukas, J. Schipper, Materials and techniques for osseous skull reconstruction. *Minim. Invasive Ther. Allied Technol.* **19**, 110–121 (2010).
44. G. R. Holt, Osseointegrated implants in oro-dental and facial prosthetic rehabilitation. *Otolaryngol. Clin. North Am.* **27**, 1001–1014 (1994).
45. A. M. Pobloth *et al*., Mechanobiologically optimized 3D titanium-mesh scaffolds enhance bone regeneration in critical segmental defects in sheep. *Sci. Transl. Med.* **10**, eaam8828 (2018).
46. M. Esposito, J. M. Hirsch, U. Lekholm, P. Thomsen, Biological factors contributing to failures of osseointegrated oral implants. (I). Success criteria and epidemiology. *Eur. J. Oral Sci.* **106**, 527–551 (1998).
47. R. Brånemark *et al*., A novel osseointegrated percutaneous prosthetic system for the treatment of patients with transfemoral amputation: A prospective study of 51 patients. *Bone Joint J.* **96-B**, 106–113 (2014).
48. D. Lindner *et al*., Cranioplasty using custom-made hydroxyapatite versus titanium: A randomized clinical trial. *J. Neurosurg.* **126**, 175–183 (2017).
49. T. Engstrand *et al*., Bioceramic implant induces bone healing of cranial defects. *Plast. Reconstr. Surg. Glob. Open* **3**, e491 (2015).
50. U. Ripamonti, L. C. Roden, C. Ferretti, R. M. Klar, Biomimetic matrices self-initiating the induction of bone formation. *J. Craniofac. Surg.* **22**, 1859–1870 (2011).
51. Z. Tang, X. Li, Y. Tan, H. Fan, X. Zhang, The material and biological characteristics of osteoinductive calcium phosphate ceramics. *Regen. Biomater.* **5**, 43–59 (2018).
52. P. Habibovic *et al*., 3D microenvironment as essential element for osteoinduction by biomaterials. *Biomaterials* **26**, 3565–3575 (2005).
53. W. Habraken, P. Habibovic, M. Epple, M. Bohner, Calcium phosphates in biomedical applications: Materials for the future? *Mater. Today* **19**, 69–87 (2016).
54. J. Persson, B. Helgason, H. Engqvist, S. J. Ferguson, C. Persson, Stiffness and strength of cranioplastic implant systems in comparison to cranial bone. *J. Craniomaxillofac. Surg.* **46**, 418–423 (2018).
55. H. Engqvist, J. Åberg, "OssDsign AB, Hydraulic cements, methods and products (13/229,539)." US Patent US20130066324A1, 1–7 (2013).
56. T. Engstrand *et al*., Development of a bioactive implant for repair and potential healing of cranial defects. *J. Neurosurg.* **120**, 273–277 (2014).
57. T. Engstrand, J. Bohlin, "OssDsign AB, Mosaic implants, kits and methods for correcting bone defects (14/179,205)." US Patent US9220597B2, 1–20 (2013).
58. K. Donath, G. Breuner, A method for the study of undecalcified bones and teeth with attached soft tissues. The Säge-Schliff (sawing and grinding) technique. *J. Oral Pathol.* **11**, 318–326 (1982).
59. M. D. Morris, G. S. Mandair, Raman assessment of bone quality. *Clin. Orthop. Relat. Res.* **469**, 2160–2169 (2011).
60. M. Kozielski *et al*., Determination of composition and structure of spongy bone tissue in human head of femur by Raman spectral mapping. *J. Mater. Sci. Mater. Med.* **22**, 1653–1661 (2011).
61. M. Kazanci *et al*., Raman imaging of two orthogonal planes within cortical bone. *Bone* **41**, 456–461 (2007).
62. A. Roschger *et al*., Relationship between the v_2PO_4/amide III ratio assessed by Raman spectroscopy and the calcium content measured by quantitative backscattered electron microscopy in healthy human osteonal bone. *J. Biomed. Opt.* **19**, 065002 (2014).
63. T. Jarmar *et al*., Technique for preparation and characterization in cross-section of oral titanium implant surfaces using focused ion beam and transmission electron microscopy. *J. Biomed. Mater. Res. A* **87**, 1003–1009 (2008).